Journal of Pharmaceutical Analysis 12 (2022) 113–121

Contents lists available at ScienceDirect

Journal of Pharmaceutical Analysis

journal homepage: www.elsevier.com/locate/jpa

Original article

Reversible regulation of enzyme-like activity of molybdenum disulfide quantum dots for colorimetric pharmaceutical analysis

Juan Tan [a], Shiyue Wu [a], Qingqing Cai [a], Yi Wang [a, *], Pu Zhang [b, **]

[a] Engineering Research Center for Biotechnology of Active Substances, Ministry of Education, Chongqing Key Laboratory of Green Synthesis and Applications, College of Chemistry, Chongqing Normal University, Chongqing, 401331, China
[b] Chongqing Research Center for Pharmaceutical Engineering, College of Pharmacy, Chongqing Medical University, Chongqing, 400016, China

ARTICLE INFO

Article history:
Received 9 September 2020
Received in revised form
24 February 2021
Accepted 25 March 2021
Available online 31 March 2021

Keywords:
Nanozyme
Aggregation
Peroxidase
Captopril
Colorimetric detection
Smartphone

ABSTRACT

Regulating the catalytic activity of nanozymes is significant for their applications in various fields. Here, we demonstrate a new strategy to achieve reversible regulation of the nanozyme's activity for sensing purpose. This strategy involves the use of zero-dimensional MoS_2 quantum dots (MQDs) as the building blocks of nanozymes which display very weak peroxidase (POD)-like activity. Interestingly, such POD-like activity of the MQDs largely enhances in the presence of Fe^{3+} while diminishes with the addition of captopril thereafter. Further investigations identify the mechanism of Fe^{3+}-mediated aggregation-induced enhancement of the POD-like activity and the inhibitory effect of captopril on the enhancement, which is highly dependent on their concentrations. Based on this finding, a colorimetric method for the detection of captopril is developed. This sensing approach exhibits the merits of simplicity, rapidness, reliability, and low cost, which has been successfully applied in quality control of captopril in pharmaceutical products. Moreover, the present sensing platform allows smartphone read-out, which has promising applications in point-of-care testing devices for clinical diagnosis and drug analysis.

1. Introduction

Inherent defects of natural enzymes including easy deactivation, low production, and high cost greatly limit their practical applications in a variety of different fields such as biomedicine, environmental pollutant treatment, and food processing [1]. Therefore, design and synthesis of artificial materials to simulate/replace natural enzymes is of great significance for enzymology and enzyme engineering. Nanozymes are a large number of artificial nanomaterials which have intrinsic natural enzyme-like characteristics [2]. Since the first example of peroxidase (POD) mimics (Fe_3O_4 nanoparticles) was reported in 2007 [3], various kinds of nanozymes such as oxidase, catalase, superoxide dismutase, and hydrolase mimics have been discovered and evaluated [4]. Sorted by elemental composition, nanozymes include noble metals (e.g., Au, Pt, Pd, and Ir) [5–9], metal oxides (e.g., CeO_{2-x}, MnO_2, Co_3O_4, and V_2O_5) [10–14], metal chalcogenides (e.g., CuS, $Cu_{2-x}Se$, and MoS_2) [15–17], carbon (e.g., graphene and carbon quantum dots) [18,19], and inorganic-organic hybrids (e.g., metal-organic frameworks and metal-organic gels) [20–22]. In contrast to their natural counterparts, nanozymes show much better stability because they are less vulnerable to denaturation and protease digestion. Moreover, nanozymes generally take advantages of low cost, mass production, and manipulated activity, which have aroused wide interest in sensing [23–26], anti-bacteria [27–29], in vitro diagnosis [30,31], environment purification [32], etc.

A number of studies have demonstrated that the catalytic efficiency of nanozymes and their selectivity toward substrate are related to physicochemical parameters of the nanomaterials such as composition, surface state, size, and shape [33]. Therefore, manipulating these parameters during their synthesis is a routine way of manipulating the enzyme-like properties and performances of nanomaterials. For instance, Luo et al. [34] found the size-dependent oxidase-like catalytic activity of gold nanoparticles in the range of 13–50 nm. Ge et al. [35] indicated that the enzyme-like activities of Pd nanocrystals are quite discrepant in different crystal facets. Xia et al. [9] engineered Pd–Ir nanocubes by depositing a few atomic layers of Ir on Pd nanocubes, which exhibited

Peer review under responsibility of Xi'an Jiaotong University.

* Corresponding author.
** Corresponding author.
E-mail addresses: ywang@cqnu.edu.cn (Y. Wang), zhangpu@cqmu.edu.cn (P. Zhang).

https://doi.org/10.1016/j.jpha.2021.03.010

significantly enhanced POD-like activity in contrast with pure Pd cubes as well as horseradish peroxidase. Recently, they also reported the strain effect-dependent activity of Pd nanozymes, where strained Pd icosahedra displayed 2-fold higher POD-like catalytic efficiency than unstrained Pd octahedra [36]. Although the catalytic activity can be tuned by screening different sizes, crystal facets, surface atoms, and internal structures of the nanozymes, people must pay much attention to the difficult synthetic technologies to obtain the nanozymes with well-defined structures. Alternatively, regulating the catalytic activity of nanozymes can also be achieved by a post-synthesis strategy. To this end, modifying the surface of nanozymes by different functional groups or charges after their synthesis has been employed to manipulate their catalytic ability. For example, Willner and co-workers [37] found that the function of β-cyclodextrin on the surface enhanced POD-like property of Cu^{2+}-carbon dots. Zhang et al. [38] achieved over 100-fold enhancement of the POD-like activity of Fe_3O_4 nanoparticles using a molecular imprinting technology to coat a specific polymer on their surfaces. In these cases, the surface coating molecules/groups can serve as the binding site of catalytic substrate to enrich them, resulting in the increase of catalytic specificity and efficiency of nanozymes. In addition, Zhao et al. [39] demonstrated the effect of surface charge on the activity of nanozymes through coating MoS_2 nanoparticles with negatively charged sodium dodecyl sulfate and positively charged hexadecyl trimethyl ammonium bromide, respectively. In spite of these achievements, most of the surface modifications are still troublesome, where complicated covalent couplings or specific host–guest molecular recognitions need to be designed and conducted.

In this work, we report a new strategy to achieve reversible regulation of the nanozyme's activity through a facile metal ion-involved approach. For our investigation, zero-dimensional MoS_2 quantum dots (MQDs) with very small sizes were prepared as the building blocks of nanozyme. Very weak POD-like catalytic activity of the MQDs was found, which could enhance over 10-fold in the presence of Fe^{3+}. Further investigations identified the mechanism of aggregation-induced enhancement of the POD-like activity. We then demonstrated that compounds involving thiols could prevent the Fe^{3+}-mediated aggregation of MQDs and thus weaken their activity again. Based on the reversibly regulated POD-like activity of MQDs under different conditions, a new colorimetric platform for captopril detection was established (Scheme 1). Captopril (CPT), an angiotensin converting enzyme inhibitor, is mainly used for clinical treatment of hypertension and congestive heart failure [40]. In addition, it is also effective for the protection of kidney function in diabetic nephropathy [41]. Therefore, quality control of CPT in different dosage forms is of great significance in clinical medication. Numerous methods including titration [42], chromatography [43], voltammetry [44], chemiluminescence [45], colorimetry [46], and fluorometry [47] have been established for quantitative detection of CPT. Nevertheless, the shortcomings such as complex pretreatment, time-consuming operation, and high cost of instruments limit their applications. Hence, developing convenient, rapid, and sensitive methods for CPT assay is still imperative and challenging. Our sensing approach based on the POD-like activity regulation exhibits the merits of simplicity, rapidness, and reliability, which also allows smartphone read-out and shows good performance in quality control of CPT tablets.

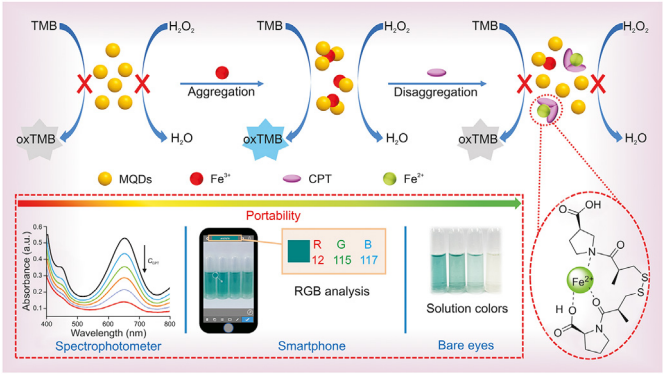

Scheme 1. Illustration of the regulating peroxidase-like activity of MoS_2 quantum dots (MQDs) with Fe^{3+} and captopril (CPT) for colorimetric detection of CPT. TMB: 3,3′,5,5′-tetramethylbenzidine; oxTMB: oxidized TMB; RGB: red, green, and blue components.

2. Experimental

2.1. Chemicals and instrumentations

Ammonium tetrathiomolybdate (≥99.0%), glucose, acetic acid (≥99.5%), sodium acetate (≥99.0%), ferric sulfate hydrate, and hydrogen peroxide (30%, *V*/*V*) were all obtained from Kelong Chemical Co., Ltd. (Chengdu, China). CPT and 3,3′,5,5′-tetramethylbenzidine dihydrochloride (TMB) were ordered from Aladdin Chemical Co., Ltd. (Shanghai, China).

A Shimadzu UV-2550 UV–vis spectrophotometer (Kyoto, Japan) was used to record absorption spectra. A Brookhaven Nano Brook Omni (New York City, NY, USA) was used to measure the size of nanoparticles in solution phase. An FEI Tecnai G2 F20 transmission electron microscope (TEM, Hillsboro, OR, USA) was employed to acquire the TEM images. A Bruker Dimension Icon atomic force microscope (AFM, Billerica, MA, USA) was used to record AFM images. A Thermo Fisher Scientific ESCALAB 250 X-ray photoelectron spectrometer (Waltham, MA, USA) was employed to obtain X-ray photoelectron spectroscopy (XPS) data. A PerkinElmer LS-55 fluorescence spectrophotometer (Waltham, MA, USA) was used to measure the fluorescence spectra. An iPhone 8 smartphone (Cupertino, CA, USA) was used for capturing the photographs of the sample solutions, and an open-source app called *Color Grab* (Shenzhen, China) was installed in the phone for data readout from the photographs.

2.2. Synthesis of MQDs

In a standard procedure, 0.05 g of $(NH_4)_2MoS_4$ was first dissolved into 10 mL of ultrapure water. After ultrasound for 10 min, 0.4 g of glucose was added into the solution. Then, the mixture was transferred to a Teflon autoclave and put in an oven (200 °C). After 8 h, the Teflon autoclave was cooled to room temperature. The MQDs were obtained by collecting supernatant after centrifugation (15,000 r/min, 15 min), and stored at 4 °C for further use.

2.3. Procedure of regulating POD-like activity of MQDs for CPT detection

In a standard procedure, CPT standard solution with different concentrations was added into a mixed solution (total volume, 3 mL) containing MQDs (100 μL), TMB (0.1 mM), H_2O_2 (10 mM), Fe^{3+} (10 μM) and acetate buffer (pH 4.0). This mixture was allowed to react at room temperature for 10 min, which was measured by a UV–vis spectrophotometer or captured/analyzed by a smartphone.

2.4. Procedure of CPT assay in tablets

Pre-treatments on the tablets were carried out before assay according to the Pharmacopoeia of the People's Republic of China (2015) [48]. In detail, 20 CPT tablets were precisely weighed and

ground into fine powder. Part of the powder (containing 10 mg of CPT) was dissolved in 100 mL of water by ultrasonic treatment. After centrifuged, supernatant was collected and further treated by filtration and dilution before the determination. Then, the sample solution was added to a mixed solution containing MQDs (100 μL), TMB (0.1 mM), H_2O_2 (10 mM), Fe^{3+} (10 μM), and acetate buffer (pH 4.0) with a total volume of 3 mL. This mixed solution was allowed to set at room temperature for 10 min before measurement.

3. Results and discussion

3.1. Characterization of MQDs

The MQDs were prepared by a hydrothermal method using $(NH_4)_2MoS_4$ and glucose as the Mo/S source and reductant, respectively [15]. A transparent solution in light yellow color was obtained. TEM images show that the MQDs were well dispersed with a narrow size distribution (~1.8 nm, Fig. S1). Highly ordered lattice fringes with spacing of 2.1 Å were observed in high-resolution TEM image, which matches with the (006) lattice of hexagonal crystal MoS_2 [49]. In addition, AFM measurement of the MQDs was performed (Fig. S2), where the monodispersity and size were consistent with those of the TEM imaging. XPS was also employed to investigate the surface chemical composition and valence states of the MQDs. As shown in high resolution Mo 3d spectrum (Fig. S3A), two characteristic peaks at 227.7 and 232.5 eV assigned to Mo $3d_{5/2}$ and Mo $3d_{3/2}$ were obtained, respectively [50]. The peaks observed at 163.4 and 164.6 eV in the S 2p spectrum were assigned to S $2p_{3/2}$ and S $2p_{1/2}$ orbitals of S^{2-}, respectively (Fig. S3B) [51]. All of these results confirmed that the QDs with composition of MoS_2 were successfully synthesized.

3.2. Regulating POD-like activity of MQDs

The POD-like activity of MQDs was studied by a typical catalytic system of POD, where TMB and H_2O_2 were employed as the substrates. Absorption spectra of the system under different conditions were measured. No characteristic peak was observed when only TMB and H_2O_2 were mixed, as shown in Fig. 1A, indicating that the oxidation of TMB by H_2O_2 was not able to occur without a catalyst (curve a). With the addition of MQDs, the absorption spectrum was almost the same as that of the mixture of TMB and H_2O_2 (curve b). It suggests that the POD-like activity of MQDs is too weak to catalyze oxidation of TMB by H_2O_2 and obtain oxidized TMB (oxTMB). Interestingly, a strong peak located at 652 nm was observed immediately when Fe^{3+} was introduced into the system (curve c), which demonstrated the formation of oxTMB. However, when CPT coexisted with Fe^{3+} in the system, the absorbance at 652 nm dramatically lowered down again (curve d). Accordingly, the solution color of TMB–H_2O_2 mixture was colorless, which had hardly any changes with the addition of MQDs. Then, it obviously changed to blue by introducing Fe^{3+} in the solution, while turned into light blue when CPT was added together with Fe^{3+} (Fig. 1B). Control experiments revealed that pure Fe^{3+} with the same concentration had very weak capability to catalyze oxidation of TMB with H_2O_2 (Fig. S4), suggesting that the formation of blue oxTMB was attributed to the strong catalytic activity of Fe^{3+}–mediated MQDs as nanozymes. Additionally, other metal ions including Na^+, K^+, Ag^+, Zn^{2+}, Mg^{2+}, Ca^{2+}, Pb^{2+}, Ni^{2+}, Co^{2+}, Hg^{2+}, Al^{3+}, and Cr^{3+} were not able to induce the aggregation of MQDs and improve their catalytic activity, while Cu^{2+} could slightly enhance their catalytic activity (Fig. S5). These results indicate that only Fe^{3+} can effectively enhance the POD-like activity of MQDs, which can be inhibited again in the presence of CPT. In other words, the Fe^{3+}–CPT pair can act as an effective mediator to manipulate the POD-like activity of MQDs. What's more, the POD-like activity of MQDs was closely related to the concentrations of Fe^{3+} and CPT. As shown in Fig. 2, the absorption at 652 nm was gradually enhanced along with increased concentration of Fe^{3+} (Fig. 2A), but decreased regularly as the concentration of CPT increased (Fig. 2B).

In order to quantify the catalytic activity and specificity of the MQDs toward POD substrate, the Michaelis–Menten behaviors of the nanozymes were further investigated. Experiments were carried out by keeping the conditions constant but only changing the

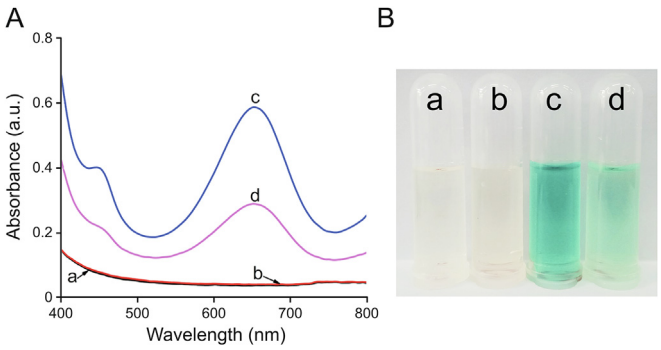

Fig. 1. (A) Typical UV–vis absorption spectra and (B) corresponding photograph of solutions containing (a) 3,3′,5,5′-tetramethylbenzidine (TMB)–H_2O_2, (b) TMB–H_2O_2 with MoS_2 quantum dots (MQDs), (c) TMB–H_2O_2 with MQDs and Fe^{3+}, and (d) TMB–H_2O_2 with MQDs, Fe^{3+}, and captopril (CPT). Concentrations of TMB, H_2O_2, Fe^{3+}, and CPT were 0.1 mM, 10 mM, 10 μM, and 60 μM, respectively.

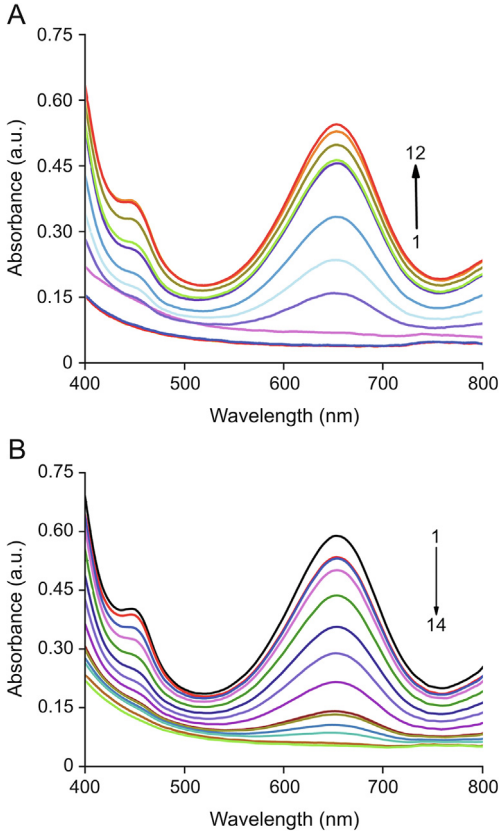

Fig. 2. The catalytic activity of MQDs regulated by different concentrations of Fe^{3+} and CPT. (A) Absorption spectra of the MQDs/TMB/H_2O_2 system with the addition of different amounts of Fe^{3+} (1–12: 0, 1, 2, 3, 4, 5, 6, 7, 9, 10, 12, and 15 μM). (B) Absorption spectra of MQDs/TMB/H_2O_2/Fe^{3+} system with the addition of different amounts of CPT (1–14: 0, 1, 10, 20, 30, 40, 50, 60, 70, 80, 90, 100, 150, and 200 μM). Concentrations of reagents: TMB, 0.1 mM; H_2O_2, 10 mM.

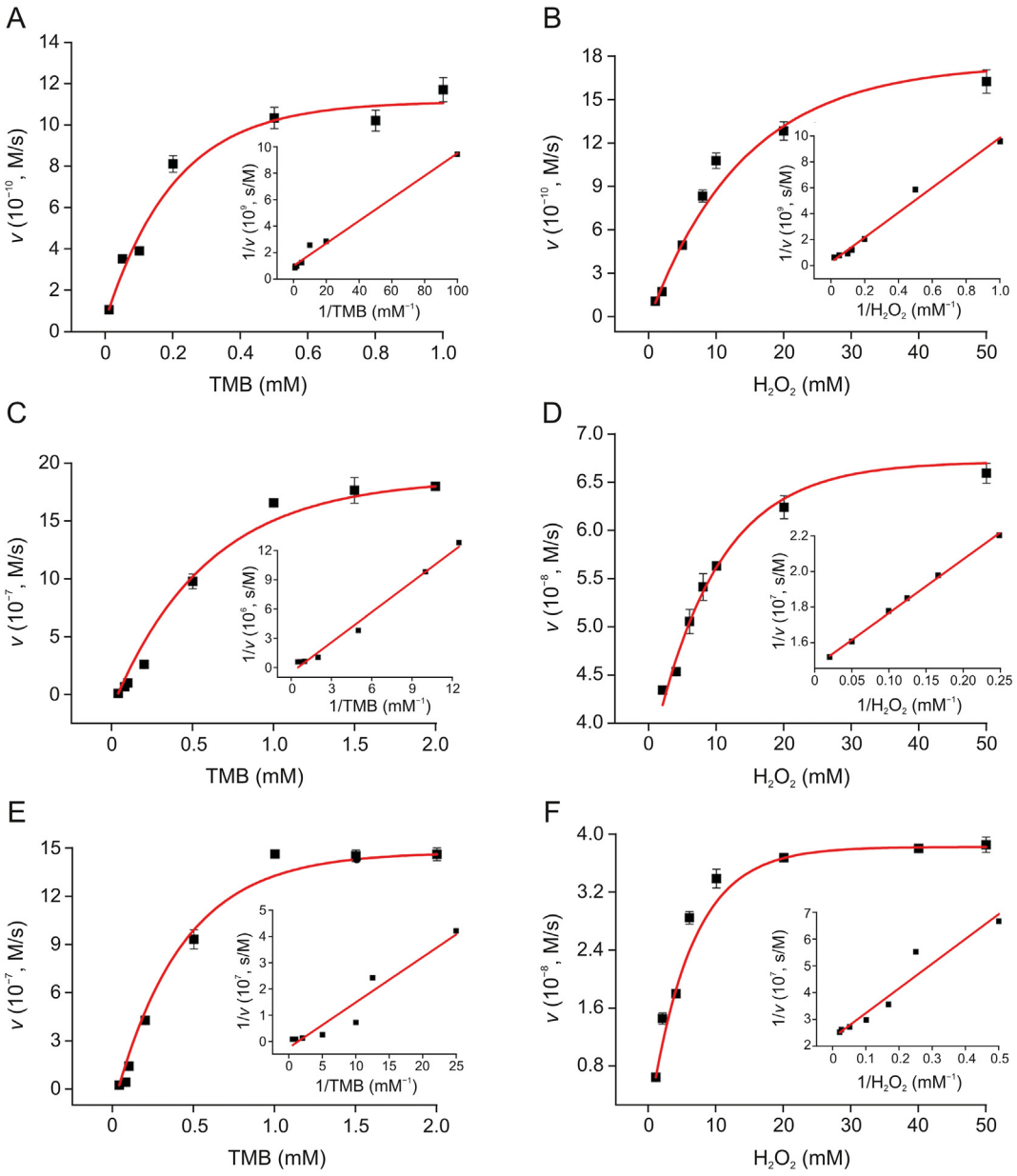

Fig. 3. Steady-state kinetics of (A and B) MQDs, (C and D) MQDs in the presence of Fe^{3+} (10 μM), and (E and F) MQDs with Fe^{3+} (10 μM) and CPT (50 μM) for catalytic oxidation of TMB by H_2O_2. The data were obtained by keeping experimental conditions constant but only varying the concentration of TMB (0.1 mM) or H_2O_2 (10 mM). Insets show the Lineweaver-Burk plots transformed from the Michaelis-Menten equations.

concentration of TMB or H_2O_2. With the increase of TMB and H_2O_2 in a certain concentration range, typical Lineweaver-Burk plots with Michaelis–Menten constant (K_m) for TMB and H_2O_2 were obtained, respectively (Fig. 3). K_m represents the affinity of an enzyme to substrates. That is, a smaller value of K_m stands for a higher affinity. Table 1 indicates that the K_m value of Fe^{3+}–MQDs nanozyme with TMB as the substrate was 11.6 times lower than that of MQDs, however, which increased 2.7 times with the addition of CPT (100 μM) in the system. Similarly, the K_m value of Fe^{3+}–MQDs nanozyme with H_2O_2 as the substrate was 18 times lower than that of MQDs, which increased 1.9 times after the addition of CPT (100 μM). In addition, either TMB or H_2O_2 as a substrate, the v_{max} values of Fe^{3+}–MQDs nanozyme were much higher than that of MQDs, which decreased again in the presence of CPT. These data demonstrated the capability of Fe^{3+} and CPT in regulating the POD-like activity of MQDs in a quantitative way.

3.3. Mechanism studies on the activity regulation of nanozymes

To explore the reason for the enhancement and decrease of POD-like activity of the MQDs by Fe^{3+} and CPT, respectively, further characterizations including fluorescence spectrometry, TEM imaging, Tyndall effect, and dynamic light scattering (DLS) measurements were carried out. Similar to other kinds of quantum dots, the as-prepared MQDs displayed blue photoluminescence due to their quantum confinement and edge effects [52]. The MQDs solution was in deep yellow color and emitted bright blue light with exposure to UV light. Fluorescent spectra showed that the maximal emission wavelength of the MQDs was at 445 nm with the excitation at 360 nm (Fig. S6A). It was also found that the fluorescence intensity of MQDs remarkably decreased in the presence of Fe^{3+}, while gradually recovered again along with increased concentration of CPT (Fig. S6B). This observation suggests that interaction

Table 1
Comparison of the kinetic parameters of the present system toward the oxidation of TMB by H_2O_2 under different conditions.

Sample	Substrate	K_m (M)	v_{max} (M/s)
MQDs	TMB	8.5×10^{-3}	1.0×10^{-9}
MQDs + Fe^{3+}	TMB	7.3×10^{-4}	1.9×10^{-6}
MQDs + Fe^{3+} + CPT	TMB	2.0×10^{-3}	4.2×10^{-7}
MQDs	H_2O_2	3.8×10^{-2}	3.9×10^{-9}
MQDs + Fe^{3+}	H_2O_2	2.1×10^{-3}	4.3×10^{-7}
MQDs + Fe^{3+} + CPT	H_2O_2	4.0×10^{-3}	6.8×10^{-8}

K_m is the Michaelis-Menten constant; v_{max} is the maximal reaction rate. MQDs: MoS_2 quantum dots; CPT: captopril; TMB: 3,3′,5,5′-tetramethylbenzidine dihydrochloride.

between MQDs and Fe^{3+} indeed occurred and CPT could suppress their interaction.

TEM images and the statistical histograms of size distribution show that the MQDs had an average size of 1.8 nm (Figs. 4A and D). Interestingly, relatively larger size (4.5 nm) was observed after the interaction between MQDs and Fe^{3+} (Figs. 4B and E), suggesting that Fe^{3+} could induce the aggregation of MQDs. However, the particle size decreased again to 2.1 nm in the presence of both Fe^{3+} and CPT (Figs. 4C and F), indicating that CPT had the capacity to prevent the Fe^{3+}–mediated aggregation of MQDs. In order to eliminate the influence of solvent drying during TEM specimen preparation, the real state of MQDs in aqueous solution was investigated by Tyndall effect and DLS. As shown in Fig. 5A, the scattering light of MQDs solution was nearly unobservable with irradiation by a laser pointer owing to their very small size. The intensity of scattering light significantly enhanced after the addition of Fe^{3+} to the MQDs solution. This phenomenon confirmed the formation of MQD aggregates with relatively large sizes in the presence of Fe^{3+}. When both Fe^{3+} and CPT were introduced, the Tyndall effect of solution largely weakened again. DLS data also revealed that the average hydrodynamic diameter of MQDs increased from ~10 nm to ~75 nm with the addition of Fe^{3+}, but lowered to ~28 nm after the introduction of CPT (Fig. 5B).

Based on these investigations, it is concluded that MQDs can be aggregated with the aid of Fe^{3+} and thus largely enhances their POD-like activity, whereas the enhancement is able to be suppressed in the presence of CPT. Since the MQDs were prepared through the reduction of $(NH_4)_2MoS_4$ by glucose, the surfaces of MQDs might be capped with large amounts of carboxyl groups from the gluconic acid generated by the oxidation of glucose. Thus, aggregates of MQDs can be formed by means of the coordination of Fe^{3+} with carboxyl groups, which might possess higher affinity for surface adsorption of TMB compared with mono-dispersed MQDs, resulting in the enhanced efficiency toward catalytic oxidation of TMB. However, the –SH group in CPT can transform Fe^{3+} into Fe^{2+} and then formation of a stable compound via coordination between Fe^{2+} and CPT [53] (Scheme 1). Therefore, the concentration of Fe^{3+} can be greatly lowered in the presence of CPT, thus inhibiting the aggregation of MQDs. This speculation was further confirmed through the replace of CPT by dithiothreitol with two –SH groups, where the POD-like activity of Fe^{3+}–MQDs also dramatically decreased (Fig. S7).

3.4. Colorimetric detection of CPT by UV–vis and smartphone

Employing Fe^{3+}–mediated MQDs nanozymes, colorimetric detection of CPT can be realized. As a mediator of the nanozyme, Fe^{3+} plays an important role in the manipulation of POD-like

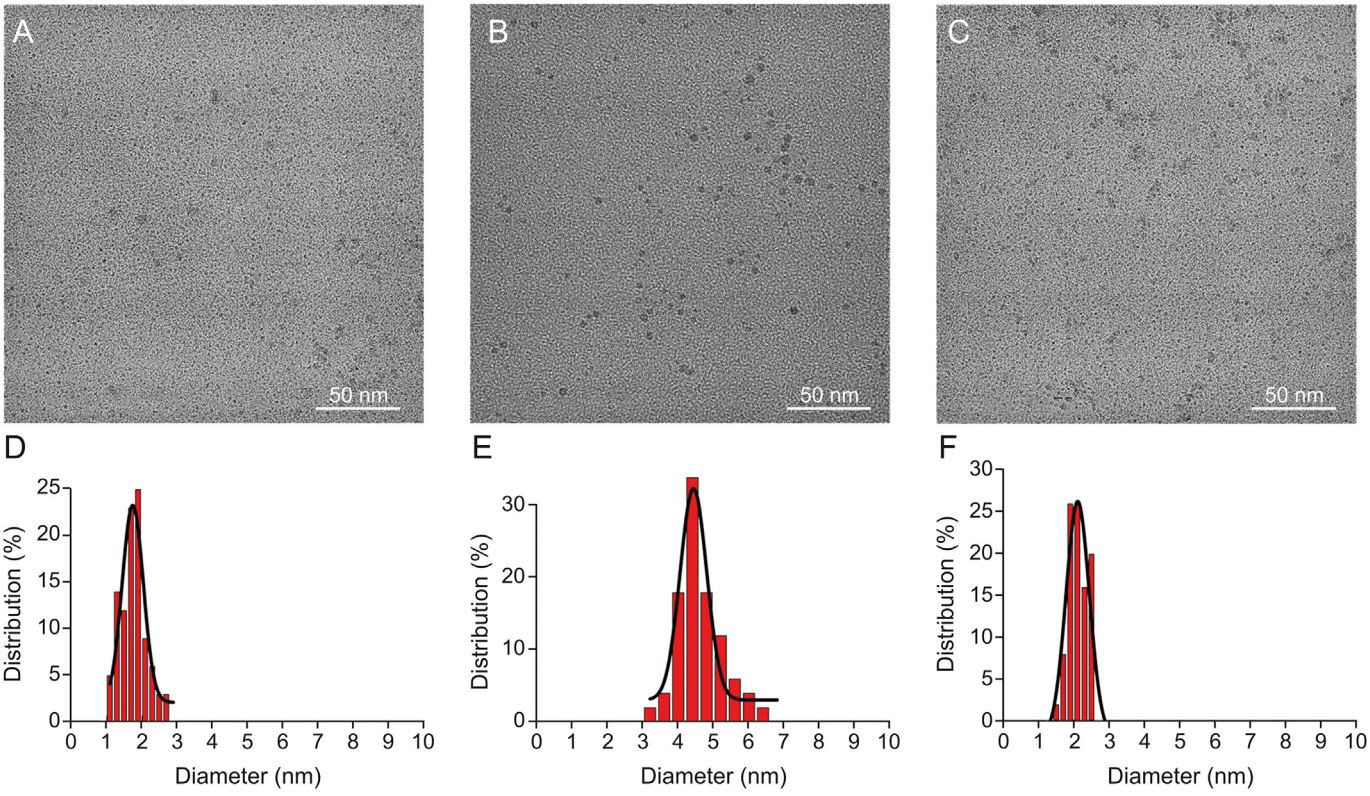

Fig. 4. Transmission electron microscope images and corresponding size distributions of (A and D) MQDs, (B and E) MQDs in the presence of Fe^{3+}, and (C and F) MQDs in the presence of Fe^{3+} and CPT.

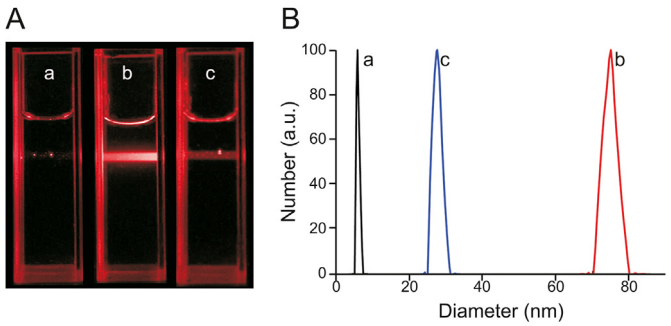

Fig. 5. (A) Tyndall effect and (B) dynamic light scattering (DLS) results of the MQDs in solution at different conditions: (a) MQDs, (b) MQDs in the presence of Fe^{3+}, and (c) MQDs in the presence of Fe^{3+} and CPT.

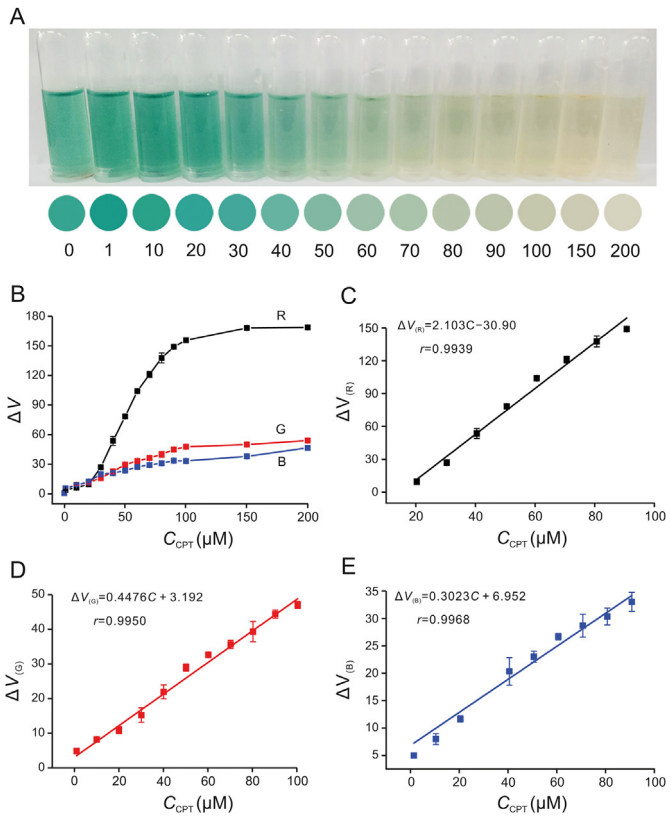

Fig. 6. Colorimetric detection of CPT using a smartphone as a readout: (A) photograph of the sample solutions with 0–200 μM of CPT; (B) the changes (Δ*V*) of R, G and B values as a function of CPT concentration; (C–E) plots of the values of ΔR, ΔG, and ΔB versus the CPT concentration, respectively.

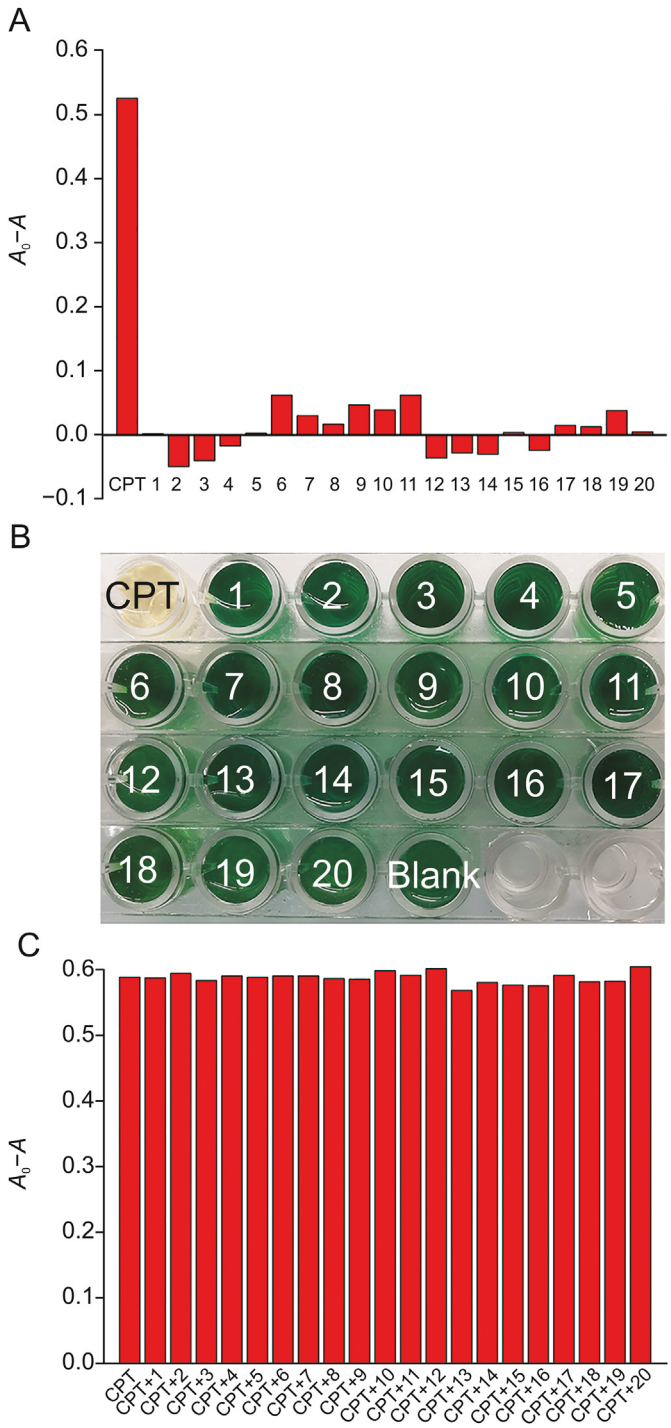

Fig. 7. Selectivity and interfering investigations of this method for CPT detection. (A) Absorbance change at 652 nm (A_0–A) when other potential interfering substances were added instead of CPT. (B) Colorimetric response of sample solutions corresponding to (A). (C) Absorbance change at 652 nm (A_0–A) when other potential interfering substances were added together with CPT. The substances numbered as 1–20: CH_3CH_2OH, Na_2CO_3, $CaCl_2$, CH_3COONa, $ZnSO_4$, $CdSO_4$, $NaHCO_3$, glucose, mannose, lysine, glutamic, threonine, valine, Na_3PO_4, $Na_2S_2O_3$, $Mg(NO_3)_2$, α-cyclodextrin, β-cyclodextrin, sucrose, and starch, respectively. Concentrations: CPT, 100 μM; substances 1–13 and 19, 1 mM; substances 14–18, 100 μM; substance 20, 500 μg/mL.

activity of the MQDs. As the concentration of Fe^{3+} increases, absorbance of the system at 652 nm is gradually increased while hardly changes when it reaches 10 μM (Fig. S8). The absorption under different pH values was also recorded, and the maximal signal change was observed at pH 4.0 (Fig. S9). Moreover, the studies on reaction kinetics showed that the absorbance at 652 nm rapidly increased within the initial 5 min and reached maximum values at about 8 min (Fig. S10). Based on these studies, the optimal conditions for the detection of CPT were obtained, namely, with the addition of 10 μM of Fe^{3+}, reacting at pH 4.0, and recording the signal after reaction for 10 min.

Under optimal experimental conditions, a facile, rapid, and cost-effective approach to the determination of CPT was proposed. Fig. 2B displays that the absorbance of the system at 652 nm decreased regularly with the increase of CPT concentration. A linear plot for CPT detection was established according to the absorbance

Table 2
Results for the quality control of captopril in tablets and the spiked recovery experiments.

Sample	Labeled amount (μM)	Measured concentration (μM)[a]		Spiked (μM)	Found (μM)	Recovery (%, n=3)	RSD (%, n=3)
		Standard method	This method				
Tablet 1[b]	25.00	24.15 ± 0.41	27.75 ± 1.78	20.00	19.27 ± 0.97	96.4	5.03
				30.00	28.95 ± 1.25	96.5	4.32
				40.00	42.74 ± 0.63	106.9	1.47
Tablet 2[c]	25.00	24.78 ± 1.86	25.81 ± 1.75	20.00	21.07 ± 0.90	105.4	4.27
				30.00	32.55 ± 1.21	108.5	3.72
				40.00	39.28 ± 0.40	98.2	1.02

[a] Titration method in the Pharmacopoeia of the People's Republic of China (2015) [48].
[b] Purchased from Shanxi Jinhua huixing pharmaceutical Co., Ltd. (Hejin, Shanxi, China).
[c] Purchased from Beijing jingfeng pharmaceutical group (Beijing, China).

change (A_0−A) at 652 nm and the CPT concentration (Fig. S11). The detectable range of this method was 20–70 μM (r=0.9998) and the limit of detection was 1.7 μM (3σ method). Compared with most previously reported methods for CPT assay (Table S1) [43,45,54–58], the proposed approach herein has higher sensitivity and comparable detection range.

In order to achieve portable detection of CPT, the smartphone was also used as the signal readout beyond that UV–vis spectrophotometry. Owing to the popularity of smartphones in people's life, they will attract increasingly attention in the future portable detection. To this end, the solution with different colors was captured by a smartphone with CPT concentration in the range of 0–200 μM (Fig. 6A). Then, red (R), green (G), and blue (B) components values of each sample in the photograph were analyzed with the help of a loaded open-source app called *Color Grab*. The changes of R, G, or B value in the absence and presence of CPT (ΔV) increased as the concentration of CPT increased at the beginning, which then reached a plateau with the addition of more than 100 μM of CPT (Fig. 6B). Linear enhancements of the ΔV were obtained in the range of 20–90 μM (r=0.9939), 1–100 μM (r=0.9950), and 1–90 μM (r=0.9968) when R, G, and B were employed as the detection signal, respectively (Figs. 6C–E). Apparently, the resolution and accuracy of the smartphone-based approach overwhelmed the visual detection by the naked eyes. Moreover, compared with the detection by UV–vis spectrophotometer, the smartphone-based strategy has the advantages of portability, flexibility, low cost, and wider detectable ranges.

3.5. Selectivity and interference studies

Selectivity of the present method for CPT assay was investigated. General species in commercially available drugs such as pharmaceutic adjuvants, saccharides, inorganic ions, and amino acid were inspected. The investigated substances were CH_3CH_2OH, Na_2CO_3, $CaCl_2$, CH_3COONa, $ZnSO_4$, $CdSO_4$, $NaHCO_3$, glucose, mannose, lysine, glutamic, threonine, valine, Na_3PO_4, $Na_2S_2O_3$, $Mg(NO_3)_2$, α-cyclodextrin, β-cyclodextrin, sucrose, and starch, respectively. Fig. 7A shows that the change of absorbance reached more than 0.5 in the presence of 100 μM CPT in the detection system, while less than ±0.1 when the CPT was replaced by other species with the same or higher concentrations. Fading of solution color was observed only for the sample involving CPT (Fig. 7B), also demonstrating the good selectivity of this approach for CPT assay. Subsequently, these substances were mixed with CPT before detection to explore the ability of this detection platform to resist interferences. Compared with that of the samples only containing CPT (100 μM), the absorbance change of the groups with the addition of both CPT and interfering species all fluctuated within 10% (Fig. 7C). Based on these findings, we can conclude that these potential interfering substances will not affect the determination of CPT in real pharmaceutical products.

3.6. CPT assay in tablets

To evaluate the practicability of this method, CPT tablets from different manufacturers were purchased and used as the real samples for assay. Pre-treatments on the tablets were carried out before assay according to the Pharmacopoeia of the People's Republic of China (2015) [48]. Finally, diluted CPT sample solutions with an appropriate concentration were obtained for assay. Each sample was measured for three times in parallel, and the standard addition experiments were conducted at the same time. As shown in Table 2, there is no significant difference between the labeled amounts and measured concentrations by the present method. Moreover, the obtained results are nearly identical with those of the standard titration method in the Pharmacopoeia of the People's Republic of China (2015) [48]. Spiked recoveries from 96.4% to 108.5% were also received, confirming the accuracy of this method and its great potential for quality control of CPT in clinical pharmaceutical products.

4. Conclusions

In conclusion, we have demonstrated that nanozyme's activity can be reversibly regulated through a facile metal ion-mediated strategy after their synthesis. That is, the POD-like activity of MQDs can be largely enhanced by Fe^{3+} owing to the Fe^{3+}-mediated aggregation of MQDs. However, such enhancement is inhibited by CPT since it can transform Fe^{3+} into Fe^{2+} and thus prevent the aggregation process of MQDs. A facile, rapid, and cost-effective colorimetric method is established for CPT detection based on the regulation of POD-like activity of MQDs, which allows us to achieve the quality control of CPT in pharmaceutical products. More importantly, it has been proven that the smartphone can also be employed as a readout and data analyzer beyond UV–vis spectrophotometer in the present method for CPT detection, which is expected to have good application prospects in clinical diagnosis and drug analysis.

CRediT author statement

Juan Tan: Investigation, Writing - Original draft preparation, Visualization; **Shiyue Wu:** Investigation, Validation; **Qingqing Cai:** Validation; **Yi Wang:** Conceptualization, Methodology, Supervision, Writing - Original draft preparation, Writing - Reviewing and Editing; **Pu Zhang:** Conceptualization, Methodology, Supervision, Writing - Original draft preparation.

Declaration of competing interest

The authors declare there are no conflicts of interest.

Acknowledgments

This work was supported by the National Natural Science Foundation of China (Grant Nos.: 21775014 and 81972020) and Open Foundation Project of Engineering Research Center for Biotechnology of Active Substances, Ministry of Education (Grant No.: AS201905). Pu Zhang and Yi Wang were sponsored by the Chongqing Talent Program (Top-notch Youth) and the Chongqing High-level Personnel of Special Support Program (Top-notch Youth), respectively.

Appendix A. Supplementary data

Supplementary data to this article can be found online at https://doi.org/10.1016/j.jpha.2021.03.010.

References

[1] H. Wei, E. Wang, Fe_3O_4 magnetic nanoparticles as peroxidase mimetics and their applications in H_2O_2 and glucose detection, Anal. Chem. 80 (2008) 2250–2254.
[2] J. Wu, X. Wang, Q. Wang, et al., Nanomaterials with enzyme-like characteristics (nanozymes): next-generation artificial enzymes (II), Chem. Soc. Rev. 48 (2019) 1004–1076.
[3] L. Gao, J. Zhuang, L. Nie, et al., Intrinsic peroxidase-like activity of ferromagnetic nanoparticles, Nat. Nanotechnol. 2 (2007) 577–583.
[4] M. Liang, X. Yan, Nanozymes: from new concepts, mechanisms, and standards to applications, Acc. Chem. Res. 52 (2019) 2190–2200.
[5] Y.J. Long, Y.F. Li, Y. Liu, et al., Visual observation of the mercury-stimulated peroxidase mimetic activity of gold nanoparticles, Chem. Commun. (Camb) 47 (2011) 11939–11941.
[6] X. Wang, W. Lv, J. Wu, et al., In situ generated nanozyme-initiated cascade reaction for amplified surface plasmon resonance sensing, Chem. Commun. (Camb) 56 (2020) 4571–4574.
[7] W. Li, B. Chen, H. Zhang, et al., BSA-stabilized Pt nanozyme for peroxidase mimetics and its application on colorimetric detection of mercury (II) ions, Biosens. Bioelectron. 66 (2015) 251–258.
[8] J. Wei, X. Chen, S. Shi, et al., An investigation of the mimetic enzyme activity of two-dimensional Pd-based nanostructures, Nanoscale 7 (2015) 19018–19026.
[9] X. Xia, J. Zhang, N. Lu, et al., Pd–Ir core–shell nanocubes: a type of highly efficient and versatile peroxidase mimic, ACS Nano 9 (2015) 9994–10004.
[10] J. Mu, Y. Wang, M. Zhao, et al., Intrinsic peroxidase-like activity and catalase-like activity of Co_3O_4 nanoparticles, Chem. Commun. (Camb) 48 (2012) 2540–2542.
[11] R. André, F. Natálio, M. Humanes, et al., V_2O_5 nanowires with an intrinsic peroxidase-like activity, Adv. Funct. Mater. 21 (2011) 501–509.
[12] Y. Li, P. Zhang, W. Fu, et al., Smartphone-based colorimetric assay of antioxidants in red wine using oxidase-mimic MnO_2 nanosheets, Analyst 144 (2019) 5479–5485.
[13] J. Wu, W. Lv, Q. Yang, et al., Label-free homogeneous electrochemical detection of MicroRNA based on target-induced anti-shielding against the catalytic activity of two-dimension nanozyme, Biosens. Bioelectron. 171 (2021), 112707.
[14] V. Baldim, F. Bedioui, N. Mignet, et al., The enzyme-like catalytic activity of cerium oxide nanoparticles and its dependency on Ce^{3+} surface area concentration, Nanoscale 10 (2018) 6971–6980.
[15] W. Xia, P. Zhang, W. Fu, et al., Aggregation/dispersion-mediated peroxidase-like activity of MoS_2 quantum dots for colorimetric pyrophosphate detection, Chem. Commun. (Camb) 55 (2019) 2039–2042.
[16] Q.J. Guo, Z.Y. Pan, C. Men, et al., Visual detection of cancer cells by using in situ grown functional $Cu_{2-x}Se$/reduced graphene oxide hybrids acting as an efficient nanozyme, Analyst 144 (2019) 716–721.
[17] Q.W. Shu, C.M. Li, P.F. Gao, et al., Porous hollow CuS nanospheres with prominent peroxidase-like activity prepared in large scale by a one-pot controllable hydrothermal step, RSC Adv. 5 (2015) 17458–17465.
[18] W. Shi, Q. Wang, Y. Long, et al., Carbon nanodots as peroxidase mimetics and their applications to glucose detection, Chem. Commun. (Camb) 47 (2011) 6695–6697.
[19] Y. Song, K. Qu, C. Zhao, et al., Graphene oxide: intrinsic peroxidase catalytic activity and its application to glucose detection, Adv. Mater. 22 (2010) 2206–2210.
[20] H. Cheng, Y. Liu, Y. Hu, et al., Monitoring of heparin activity in live rats using metal–organic framework nanosheets as peroxidase mimics, Anal. Chem. 89 (2017) 11552–11559.
[21] J. Wang, Y. Hu, Q. Zhou, et al., Peroxidase-like activity of metal–organic framework [Cu(PDA)(DMF)] and its application for colorimetric detection of dopamine, ACS Appl. Mater. Interfaces 11 (2019) 44466–44473.
[22] L. He, Y. Li, Q. Wu, et al., Ru(III)-based metal–organic gels: intrinsic horseradish and NADH peroxidase-mimicking nanozyme, ACS Appl. Mater. Interfaces 11 (2019) 29158–29166.
[23] L.-N. Zhang, H.-H. Deng, F.-L. Lin, et al., In situ growth of porous platinum nanoparticles on graphene oxide for colorimetric detection of cancer cells, Anal. Chem. 86 (2014) 2711–2718.
[24] Z. Gao, G.G. Liu, H. Ye, et al., Facile colorimetric detection of silver ions with picomolar sensitivity, Anal. Chem. 89 (2017) 3622–3629.
[25] Z. Gao, S. Lv, M. Xu, et al., High-index {hk0} faceted platinum concave nanocubes with enhanced peroxidase-like activity for an ultrasensitive colorimetric immunoassay of the human prostate-specific antigen, Analyst 142 (2017) 911–917.
[26] Y. Wang, P. Zhang, L. Liu, et al., Regulating peroxidase-like activity of Pd nanocubes through surface inactivation and its application for sulfide detection, New J. Chem. 43 (2019) 371–376.
[27] B. Xu, H. Wang, W. Wang, et al., A single-atom nanozyme for wound disinfection applications, Angew. Chem. Int. Ed. Engl. 58 (2019) 4911–4916.
[28] L. Huang, J. Chen, L. Gan, et al., Single-atom nanozymes, Sci. Adv. 5 (2019), eaav5490.
[29] J. Shan, X. Li, K. Yang, et al., Efficient bacteria killing by Cu_2WS_4 nanocrystals with enzyme-like properties and bacteria-binding ability, ACS Nano 13 (2019) 13797–13808.
[30] Z. Xi, H. Ye, X. Xia, Engineered noble-metal nanostructures for in vitro diagnostics, Chem. Mater. 30 (2018) 8391–8414.
[31] Z. Gao, H. Ye, D. Tang, et al., Platinum-decorated gold nanoparticles with dual functionalities for ultrasensitive colorimetric in vitro diagnostics, Nano Lett. 17 (2017) 5572–5579.
[32] Z. Sui, Q. Meng, X. Zhang, et al., Green synthesis of carbon nanotube–graphene hybrid aerogels and their use as versatile agents for water purification, J. Mater. Chem. 22 (2012) 8767–8771.
[33] Y. Huang, J. Ren, X. Qu, Nanozymes: classification, catalytic mechanisms, activity regulation, and applications, Chem. Rev. 119 (2019) 4357–4412.
[34] W. Luo, C. Zhu, S. Su, et al., Self-catalyzed, self-limiting growth of glucose oxidase-mimicking gold nanoparticles, ACS Nano 4 (2010) 7451–7458.
[35] C. Ge, G. Fang, X. Shen, et al., Facet energy versus enzyme-like activities: the unexpected protection of palladium nanocrystals against oxidative damage, ACS Nano 10 (2016) 10436–10445.
[36] Z. Xi, X. Cheng, Z. Gao, et al., Strain effect in palladium nanostructures as nanozymes, Nano Lett. 20 (2020) 272–277.
[37] M. Vázquez-González, W.-C. Liao, R. Cazelles, et al., Mimicking horseradish peroxidase functions using Cu^{2+}-modified carbon nitride nanoparticles or Cu^{2+}-modified carbon dots as heterogeneous catalysts, ACS Nano 11 (2017) 3247–3253.
[38] Z. Zhang, X. Zhang, B. Liu, et al., Molecular imprinting on inorganic nanozymes for hundred-fold enzyme specificity, J. Am. Chem. Soc. 139 (2017) 5412–5419.
[39] K. Zhao, W. Gu, S. Zheng, et al., SDS–MoS_2 nanoparticles as highly-efficient peroxidase mimetics for colorimetric detection of H_2O_2 and glucose, Talanta 141 (2015) 47–52.
[40] B.A. Dickinson, H.M. Semus, R.L. Montgomery, et al., Plasma microRNAs serve as biomarkers of therapeutic efficacy and disease progression in hypertension-induced heart failure, Eur. J. Heart Fail. 15 (2013) 650–659.
[41] P. Chen, H. Lao, F. Qu, et al., Ratiometric captopril assay based on the recovery of the Bi (III)-quenched yellow fluorescence of dually emitting carbon nanodots, New J. Chem. 41 (2017) 2227–2230.
[42] E. Schmidt Jr., W.R. Melchert, F.R.P. Rocha, Flow-injection iodimetric determination of captopril in pharmaceutical preparations, J. Braz. Chem. Soc. 20 (2009) 236–242.
[43] S. Vancea, S. Imre, G. Donáth-Nagy, et al., Determination of free captopril in human plasma by liquid chromatography with mass spectrometry detection, Talanta 79 (2009) 436–441.
[44] G. Absalan, M. Akhond, R. Karimi, et al., Simultaneous determination of captopril and hydrochlorothiazide by using a carbon ionic liquid electrode modified with copper hydroxide nanoparticles, Microchim. Acta 185 (2018), 97.
[45] Q. Chen, S. Bai, C. Lu, The new approach for captopril detection employing triangular gold nanoparticles-catalyzed luminol chemiluminescence,, Talanta 89 (2012) 142–148.
[46] C.G. Ravazzi, M.O. Krambeck Franco, M.C.R. Vieira, et al., Smartphone application for captopril determination in dosage forms and synthetic urine employing digital imaging, Talanta 189 (2018) 339–344.
[47] S.J. Xiao, X.J. Zhao, Z.J. Chu, et al., New ofi–on sensor for captopril sensing based on photoluminescent MoO_x quantum dots, ACS Omega 2 (2017) 1666–1671.
[48] Chinese Pharmacopoeia Commission, Pharmacopoeia of the People's Republic of China, China Medical Science Press, Beijing, 2015.
[49] W. Gu, Y. Yan, C. Zhang, et al., One-step synthesis of water-soluble MoS_2 quantum dots via a hydrothermal method as a fluorescent probe for hyaluronidase detection, ACS Appl. Mater. Interfaces 8 (2016) 11272–11279.
[50] W. Gao, M. Wang, C. Ran, et al., Facile one-pot synthesis of MoS_2 quantum dots–graphene–TiO_2 composites for highly enhanced photocatalytic properties, Chem. Commun. (Camb) 51 (2015) 1709–1712.
[51] X. Ren, L. Pang, Y. Zhang, et al., One-step hydrothermal synthesis of monolayer MoS_2 quantum dots for highly efficient electrocatalytic hydrogen evolution, J. Mater. Chem. A 3 (2015) 10693–10697.
[52] N. Sabari Arul, V.D. Nithya, Molybdenum disulfide quantum dots: synthesis and applications, RSC Adv. 6 (2016) 65670–65682.
[53] Y. Shi, J. Peng, X. Meng, et al., Turn-on fluorescent detection of captopril in

urine samples based on hydrophilic hydroxypropyl β-cyclodextrin polymer, Anal. Bioanal. Chem. 410 (2018) 7373–7384.
[54] C.A.T. Toloza, S. Khan, R.L.D. Silva, et al., Different approaches for sensing captopril based on functionalized graphene quantum dots as photoluminescent probe, J. Lumin. 179 (2016) 83–92.
[55] H. Bahramipur, F. Jalali, Voltammetric determination of captopril using chlorpromazine as a homogeneous mediator, Int. J. Electrochem 2011 (2011), 864358.
[56] F. Armijo, I. Torres, R. Tapia, et al., Captopril electrochemical oxidation on fluorine-doped SnO_2 electrodes and their determination in pharmaceutical preparations, Electroanalysis 22 (2010) 2269–2276.
[57] W.T. Suarez, O.D. Pessoa-Neto, B.C. Janegitz, et al., Flow injection spectrophotometric determination of N-acetylcysteine and captopril employing prussian blue generation reaction, Anal. Lett. 44 (2011) 2394–2405.
[58] B. Pasquini, S. Orlandini, C. Caprini, et al., Cyclodextrin-and solvent-modified micellar electrokinetic chromatography for the determination of captopril, hydrochlorothiazide and their impurities: a quality by design approach, Talanta 160 (2016) 332–339.